

Anomalous yaw torque generation from passively pitching wings

Nick Gravish and Robert J. Wood

Abstract—Small, lightweight micro-aerial vehicles (MAVs) must rely on a limited number of actuators for flight stability and control. A method for six-degree of freedom control in a dual-actuator MAV has been previously proposed which employs stroke amplitude, bias, and split-cycle timing modulation. This control scheme is the basis of actuation for stable, controlled flapping wing flight of the Harvard Robobee. The role of passive wing pitching dynamics are currently unexplored in their effects on yaw-dynamics during free flight. Here we demonstrate in simulation and experiment the critical role wing pitching dynamics play in yaw control of a dual-actuated MAV using the split-cycle control scheme. We find that yaw-authority sensitively depends on the functional form of the wing hinge joint and that pitching dynamics of wing hinges with linear stiffness may compromise yaw control. To solve this we present a design method for laminate based non-linear hinges and demonstrate that non-linear hinge stiffness improves yaw torque generation during split-cycle actuation.

I. INTRODUCTION

Lightweight actuation is at a premium for milli- and micro-scale robots [1], [2]. Nowhere is this more important than for micro-aerial vehicles (MAVs) in which flight-dynamics are fast, and payload is minimal [3]. A control method for stable flapping wing flight of micro-aerial vehicles has been previously proposed which uses a single actuator per wing to modulate body forces and torques [4]. This method has been demonstrated in benchtop experiments, and is the basis of stable, controlled free-flight of the dual-actuator robobee (DAB), an 80 mg dual-actuated flapping wing robot [5], [6](Fig. 1).

Dual-actuator control of flapping wing MAVs is achieved through independent modulation of stroke amplitude, bias, and upstroke-downstroke timing (split-cycle modulation). The dual-actuator robobee is capable of generating roll, pitch, and yaw body torques through amplitude, bias, and split-cycle modulation [5]. However, experiments demonstrate that yaw-authority is the weakest control axis in robobee split-cycle actuation [6]. A potential source of reduced yaw control may be from the passive wing flexibility implemented in robobee wing hinges. Simulations have recently shown that wing flexibility can destabilize the split-cycle yaw control scheme [7], yet an understanding of the dynamical basis for this instability, and experimental validation are lacking.

In the dual-actuator torque generation scheme, roll and pitch torques are generated through antagonistic (roll) or offset (pitch) *lift* forces across the wings. Yaw torque is generated through differential wing *drag* [4], [6]. Therefore, understanding how to generate predictable and large drag

forces from flexible wings is essential to optimizing split-cycle yaw control.

Previous modeling approaches for split-cycle control have assumed a constant drag coefficient during the wing-stroke, but have not included models of wing-flexibility, or resonant system dynamics of the robot [5], [4]. We hypothesize that wing flexibility will act to undermine yaw control authority during split-cycling. Initial evidence can be seen from three-dimensional simulations of passively pitching, flapping wings [8] in which increasing the split-cycle control parameter results in asymmetric wing pitch (and potentially drag) across the stroke (Fig. 1c).

To address the issue of yaw torque generation with flexible flapping wings, we study the passive pitching dynamics of a split-cycle actuated MAV. We demonstrate that yaw torque during split-cycle actuation is sensitive to wing pitch dynamics, and that linear stiffness wing hinges inhibit yaw torque generation due to the passive wing pitch. Furthermore, for flexible wings the direction of yaw torque generation during split-cycling is opposite the direction expected from a rigid wing model. To overcome this discrepancy, we construct two- and three-dimensional models to explain the anomalous yaw torque observed during passive wing pitching. Lastly, we construct laminate hinges with controllable non-linear stiffness profiles to resist bending under aerodynamic loads. We demonstrate in experiment that anomalous yaw torques are generated by flexible wings and that variations in wing stiffness, and stiffness profile can act to restore the expected

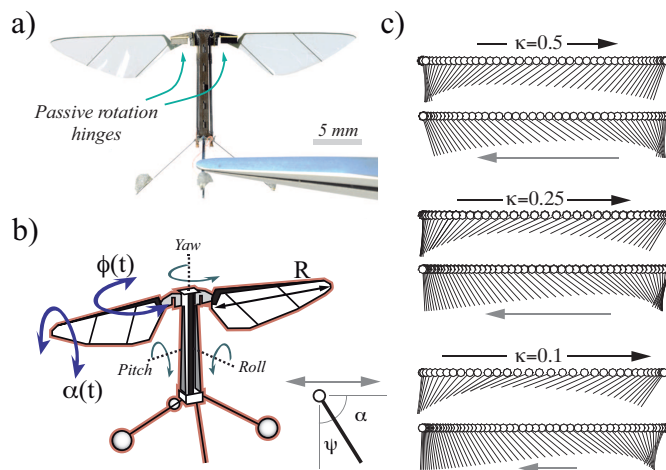


Fig. 1. a) The robobee and passive flexure wing hinges. b) Axis definitions. Inset shows definition of α and ψ . c) Snapshots of the upstroke and downstroke of the projected wing position and pitch from 3D simulation. Wing kinematics for symmetric ($\kappa = 0.5$) and split-cycle actuation ($\kappa \neq 0.5$).

yaw torque control authority.

II. MODELING

Split-cycle actuation relies on separating the constant period wing-stroke into a fast and slow phase. During the fast upstroke (or downstroke respectively) larger drag-force is generated compared to the slow downstroke (upstroke) and thus a cycle-averaged net drag force is generated (Fig. 1c). Split-cycling the left and right wings oppositely is expected to generate a mean yaw torque about the body axis. However, wings with passive pitch hinge rotation may complicate this process. To maximize yaw control-authority for passively pitching wings we need to understand how pitch dynamics influence torque generation. Wing pitch, α , is typically defined with respect to the horizontal (Inset Fig. 1b). Here we define the angle, ψ , to represent the hinge angle about the neutral position such that $\psi = \frac{\pi}{2} - \alpha$. Further references to wing pitch in this study refer to the angle about the vertical, ψ .

A. Translational model

To gain intuition for the control problem, we first analyze the passive pitch dynamics during split cycling using a translational, quasi-steady aerodynamic model (a full three-dimensional model is implemented in section II-C). The challenge of split-cycle yaw control for passively pitching wings results from the fact that passive pitch angle is a function of wing velocity, since in the quasi-steady case pitch torque is balanced by aerodynamic force. Aerodynamic force on the wing at pitch angle ψ , and translational velocity \dot{x} is modeled by the following,

(1)

$$F_L(\psi, \dot{x}) = \frac{1}{2} \rho C_L(\psi) A \dot{x}^2 \quad (2)$$

quasi-steady method [9], [10] in which lift and drag forces are $F_L(\psi, \dot{x})$, and $F_D(\psi, \dot{x})$ respectively. Lift and drag are proportional to fluid density, ρ , wing area, A , velocity squared, and lift and drag coefficients C_L and C_D which are themselves functions of wing pitch angle [11], [8] given by

$$C_D(\psi) = 1.9 - 1.5 \cos(2[\frac{\pi}{2} - \psi]) \quad (3)$$

$$C_L(\psi) = 1.8 \sin(2[\frac{\pi}{2} - \psi]) \quad (4)$$

For a passively pitching wing at steady-state velocity \dot{x}_{ss} , the force balance equation is

$$k(\psi)\psi = Fr_{cp} \quad (5)$$

where r_{cp} is the location of the wing center of pressure (typically $\frac{1}{4}$ chord length for thin, translating airfoils) and $k(\psi)$ is a generalized stiffness profile for the wing hinge ($k(\psi) = k_0$ for a linear spring). The force, F , acts perpendicular to the wing face and is thus a combination of lift and drag terms as follows,

$$F = \frac{1}{2} \rho A \dot{x}_{ss}^2 [\sin(\psi)C_L(\psi) + \cos(\psi)C_D(\psi)] \quad (6)$$

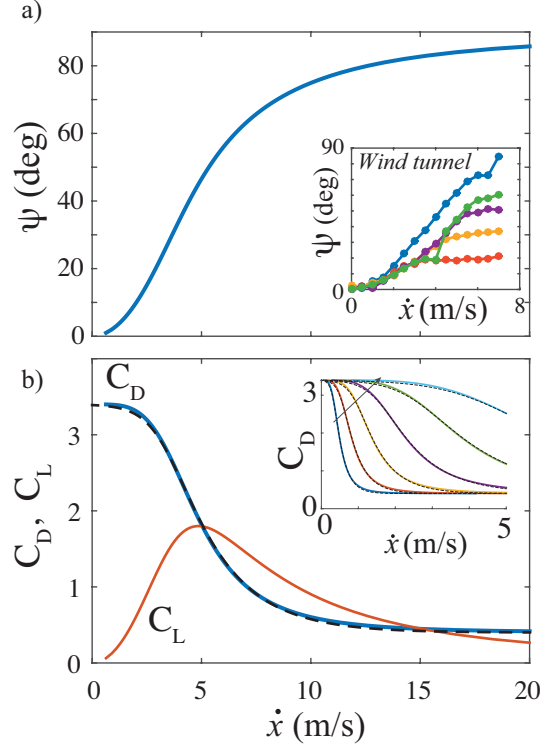


Fig. 2. Quasi-steady hinge angle and coefficient of drag for a passively pitching wing in translation. Inset shows wind measurements from hinges described in section III. b) Lift and drag coefficients for a passively pitching wing in translation. Dashed line is fit function described in text. Inset in (b) shows C_D curves for increasing values of hinge stiffness (i.e. decreasing dimensionless parameter β).

We re-write the force balance to relate steady-state wing velocity with wing pitch angle as

$$\dot{x}_{ss} = \sqrt{\frac{2k(\psi)\psi}{\rho A r_{cp} [\sin(\psi)C_L(\psi) + \cos(\psi)C_D(\psi)]}} \quad (7)$$

For a linear stiffness hinge, $k(\psi) = k_0$, a further simplification can be made by rescaling velocity by the parameter, $\beta = \sqrt{\frac{\rho A r_{cp}}{k_0}}$, which represents the force balance between aerodynamic pressure and restoring elastic force. Thus equation 7 reduces to

$$\dot{x}_{ss} = \beta [(\sin(\psi)C_L(\psi) + \cos(\psi)C_D(\psi))]^{-1/2} \quad (8)$$

Solving equation 8 for pitch angle as a function of velocity, $\psi(\dot{x}_{ss})$, we find that ψ increases monotonically from a vertical to horizontal orientation with increasing velocity (Fig. 2a). Substitution of $\psi(\dot{x}_{ss})$ into equations 3 & 4 reveals the functional dependence of lift and drag coefficients on velocity under steady-state passive wing pitching conditions (Fig. 2b).

With increasing steady-state velocity the wing pitches to higher angles which result in a monotonically decreasing drag coefficient (Fig. 2). The lift coefficient increases from zero at low velocity to a maximum value at intermediate velocity, and a subsequent decrease again as velocity increases. We model the functional form of C_D using a fit

function $C_D(\dot{x}) = 3 \left[1 - \frac{1}{1 + \exp[-\varepsilon(\dot{x} - (4.5951/\varepsilon))]} \right] + .4$ with two free parameters γ and ε which model the shape and decay of the curve. Over a wide range of hinge stiffnesses we find that $\gamma = 0.3093$ and that ε scales linearly with β . Thus as we increase hinge stiffness (or decrease aerodynamic load), $C_D(\dot{x})$ remains large over a large velocity range (i.e. the wing resists rotation). Having now gained some intuition for the passive pitching dynamics under steady-state translation, we incorporate this into our model for yaw torque generation in split-cycle actuation.

B. Quasi-steady split-cycle dynamics with passive wing pitch

We now consider the case of split-cycle actuation for passively pitching wings, again restricting our analysis to translating wings for simplicity. Consider a wing of area A , attached to a rotational hinge at the root (at $x(t)$) with stiffness $k(\psi)$, subject to oscillatory translation of the wing base at frequency ω (period $T = \frac{2\pi}{\omega}$). When the stroke cycle is split into a high-speed cycle of duration κT , and a low-speed cycle of duration $T(1 - \kappa)$, with $0 < \kappa < 1$ defined as the split-cycle control parameter, the stroke kinematics are as follows

$$x(t) = A \cdot \begin{cases} \cos\left(\frac{\omega t}{2\kappa}\right) & 0 < t \leq \kappa \frac{2\pi}{\omega} \\ \cos\left(\frac{\omega t - \pi}{2(1-\kappa)}\right) & \kappa \frac{2\pi}{\omega} \leq t < \frac{2\pi}{\omega} \end{cases} \quad (9)$$

$$\dot{x}(t) = A \cdot \begin{cases} -\frac{a\omega}{2\kappa} \sin\left(\frac{\omega t}{2\kappa}\right) & 0 < t \leq \kappa \frac{2\pi}{\omega} \\ -\frac{a\omega}{2(1-\kappa)} \sin\left(\frac{\omega t - \pi}{2(1-\kappa)}\right) & \kappa \frac{2\pi}{\omega} \leq t < \frac{2\pi}{\omega} \end{cases} \quad (10)$$

Yaw torque through split-cycling is generated by development of a mean drag force on the wing over a stroke period which can be represented as

$$\overline{F_D} = \frac{1}{T} \left[\int_0^{\kappa T} F_{D,up}(\dot{x}_{up}) - \int_{\kappa T}^T F_{D,down}(\dot{x}_{down}) \right] \quad (11)$$

$$= \frac{\rho A}{2T} \left[\int_0^{\kappa T} C_D(\dot{x}_{up}) \dot{x}_{up}^2 - \int_{\kappa T}^T C_D(\dot{x}_{down}) \dot{x}_{down}^2 \right] \quad (12)$$

where yaw torque is

$$\tau = 2r_{cp} \overline{F_D} \quad (13)$$

For situations in which wing kinematics are prescribed and symmetric over the stroke cycle, a valid modeling simplification is to assume constant stroke averaged drag coefficient $C_D(\psi) = C_{D,0}$. In this case equation 13 can be integrated analytically, resulting in the control relationship

$$\tau(\kappa) = C_0 r_{cp} \pi A^2 \omega \frac{2\kappa - 1}{4\kappa(\kappa - 1)} \quad (14)$$

Equation 14 demonstrates the expected result, that variation in split cycle timing yields variation in output torque (Fig. 3).

A problem is revealed when we evaluate the yaw torque generated through split-cycle actuation when we allow for a

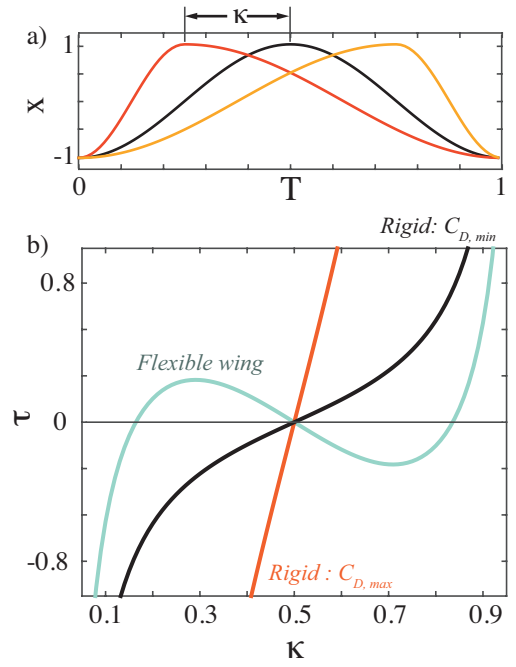


Fig. 3. a) Examples of split-cycle trajectories. b) yaw torque control relationship for fixed C_D (both maximum and minimum values of shown) flapped at a velocity that maximizes $F_L(\dot{x})/F_D(\dot{x})$ at $\kappa = 0$. Yaw torque is normalized by the parameter β .

passively pitching wing; increasing κ up or down around the equilibrium value of $\kappa = 0.5$ results in yaw torques opposite the sign expected from a constant C_D model (blue curve in Fig. 3a). The operating point for the flexible wing curve in Figure 3 was chosen to maximize the lift-to-drag ratio for the given wing size and hinge combination.

If we evaluate the yaw torque control curves at different steady-state velocities (which correspond in practice to different operating frequencies) we find that the split-cycle control relationship changes significantly (Fig. 4a). Curves on top and bottom of Figure 4a show snapshots of the yaw torque, split-cycle relationship at a given lift-to-drag operating point. We see that near operating points of high lift-to-drag ratio, like those that would be chosen for a flapping wing MAV, the yaw control relationship for flexible wings is opposite the predictions from a simplified constant C_D model.

We measure the linearized slope of $\tau(\kappa)$ about the equilibrium control value of $\kappa = 0.5$ (Fig. 4b). At low F_L/F_D yaw torque authority $\frac{\partial \tau}{\partial \kappa}$ can be either zero (when $\dot{x} \rightarrow 0$, hence $\psi \rightarrow 0$) or positive and large (when $\dot{x} \rightarrow \infty$ and $\psi \rightarrow 90^\circ$). As F_L/F_D increases we observe a bifurcation in torque control authority with the equilibrium slope switching sign and becoming negative. At an operating point that maximizes F_L/F_D , such as one that might be chosen for a flight-capable vehicle, we observe the maximal negative relationship between yaw control and split-cycle control signal.

This quasi-steady analysis highlights a potentially deep yaw control problem for flapping wing robots that use

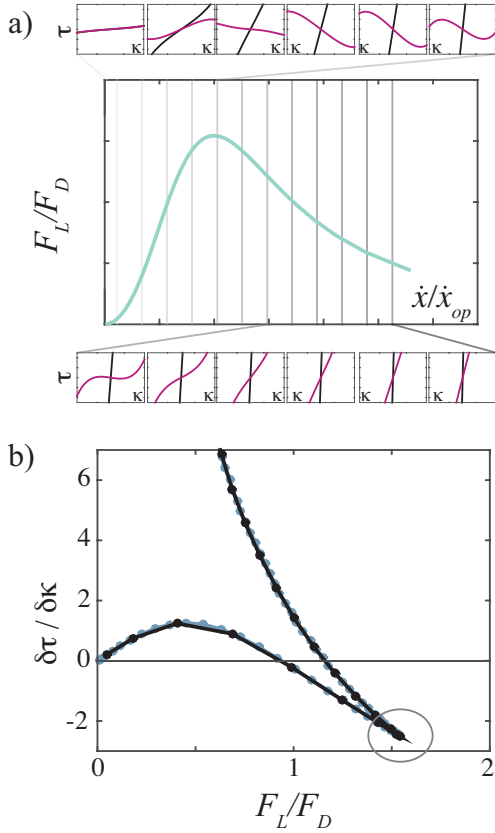


Fig. 4. Yaw control dynamics at operating points with varied F_L/F_D . (a) Center plot shows F_L/F_D versus velocity, normalized by the velocity which maximizes lift-to-drag. Vertical lines correspond to snapshots where we evaluate the yaw control curves $\tau(\kappa)$ shown above and below. The six $\tau(\kappa)$ plots above shows evolution of τ as F_L/F_D increases from zero. Bottom six $\tau(\kappa)$ plots shows evolution of τ as F_L/F_D decreases from max value. (b) Linearized slope of $\tau(\kappa)$ about the equilibrium operating point, $\kappa = 0.5$ versus F_L/F_D . Circle highlights the operating point of the flexible wing yaw control plotted in Fig. 3.

passive, linear spring hinges. In the best case, operating far from maximal lift-to-drag yaw control may be large however such an operating point is likely to be inefficient from a power perspective. In the worst case, choosing an operating frequency that exactly maximizes the lift-to-drag ratio results in yaw control dynamics which are opposite what would be expected for a yaw control model based on constant $C_D(\psi)$, and that may be very sensitive to changes in stroke kinematics from other control inputs (such as amplitude and bias modulation).

C. Three-dimensional simulation

Our consideration of yaw control dynamics under split-cycle actuation has so far focused only on quasi-steady modeling in which wing-inertia and system actuator dynamics do not factor in. For realistic flapping wing vehicle design however these parameters significantly influence flight and control dynamics. We thus implement a three-dimensional simulation of wing dynamics under split-cycle actuation. We follow the passive wing modeling of Whitney & Wood [8] (see paper for details) incorporating in a fixed torque

| | | | |
|-----------------|---------------------------------|----------------------|--------------------|
| $k_{act-trans}$ | Actuator-transmission stiffness | 3.6×10^{-5} | N m / rad |
| M_{max} | Maximum actuator torque | 1.8×10^{-5} | N m |
| k_{hinge} | Base hinge stiffness | 1.5×10^{-6} | N m / rad |
| I_{yy} | Inertia about stroke plane | 0.889 | mg mm ² |
| I_{xx} | Inertia about pitch axis | 13.73 | mg mm ² |
| I_{xy} | Off-axis moment of inertia | 0.069 | mg mm ² |
| R | Wing radius | 15 | mm |

TABLE I
TABLE OF SIMULATION PARAMETERS.

source for actuation, rather than the fixed kinematics approach previously employed. We integrate the rigid body equations of motion for a thin wing allowed to passively rotate with controllable wing hinge stiffness, $k(\psi)$. We model the aerodynamic loading of the wing using quasi-steady aerodynamics applied to the rotating wing system, however we do not consider added mass or rotational damping in this model. Wing stroke angle, $\phi(t)$ is actuated through a torque limited actuator pair such that the wing experiences a cyclic torque of

$$M_{actuator}(t) = M_{max} \cdot \begin{cases} \cos\left(\frac{\omega t}{2\kappa}\right) & 0 < t \leq \kappa \cdot \frac{2\pi}{\omega} \\ \cos\left(\frac{\omega t - s\pi}{2(1-\kappa)}\right) & \kappa \cdot \frac{2\pi}{\omega} \leq t < \frac{2\pi}{\omega} \end{cases} \quad (15)$$

with the total torque about the stroke axis being the combination of actuator input torque, aerodynamic torque, and a restoring torque from the elasticity of the actuator-transmission pair. Thus the total moment about the wing stroke dynamics is given by the following equation

$$M_\phi = M_{actuator}(t) + F_D(t) - k_{act-trans}\phi \quad (16)$$

where F_D is defined as always being opposite $\dot{\phi}$. We integrate the equations of motion to solve for wing kinematics. Simulation parameters are chosen to match measured and calculated values from experiments (see table 1).

We performed simulations across varied flapping frequency, passive hinge stiffness, and hinge stiffness values.

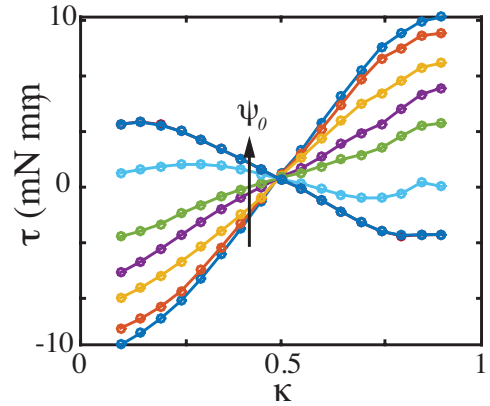


Fig. 5. Yaw-authority from full three-dimensional simulation with quasi-steady aerodynamics. Flexible wings with a variable stop angle are simulated and yaw control is shown here. Hinge stop-angles increase from 30° to 90° increasing in the direction of the arrow.

Our simulation has been previously demonstrated to match flapping wing kinematics and forces for passive pitching wings [10]. Consistent with robobee experiments, flapping wing dynamics were frequency dependent and exhibited resonant lift and stroke-amplitude behavior. The resonant frequency may be varied by changing system stiffness, wing inertia, and damping properties. To maximize payload capacity, the robobee is typically operated near maximum lift-to-drag ratio (which results in a stroke averaged angle of approximately 50°). At operating frequencies consistent with the robobee operating frequencies in experiment, we find that wing flexibility has a non-monotonic effect on yaw torque generation (Fig. 5) validating our simplified translational model of section II-B.

To circumvent anomalous yaw torque control for flexible, flapping wing MAVs we implement in simulation wing hinges with non-linear stiffness profiles. Hinge stops have been implemented in other flapping wing vehicles [4], [12], however the design choices and dynamical consequences surrounding nonlinear wing hinges have not been fully investigated. We simulate non-linear hinges as a two-slope curve which transitions from slope, k_1 to slope, k_2 at an angle ψ_0 . We find that for increasing ψ_0 , yaw control relationship transitions from the prediction of constant C_D (at $\psi_0 = 0$) to that of a fully flexible wing (at $\psi = 180$).

III. DESIGN AND MANUFACTURING

We construct nonlinear wing hinges for the robobee to explore the consequences of flexible wings on yaw control. Previously proposed mechanisms for split-cycle actuation have suggested hinge stops to limit wing motion [4]. Hinge stops based on interference between structural layers near the hinge may become impractical however as feature size decreases: 1) they rely on out-of plane geometry which is less precise in the laminate pop-up robotics process, 2) hinge length is coupled to flexure elasticity and thus may limit the interference hinge geometries available for a given stiffness, 3) interference hinges operating at high frequency may induce large joint stress leading to rapid failure. To circumvent these effects, we design soft-stop flexure hinges with variable stiffness profiles.

Our hinge design consists of patterned flexure, structural, and adhesive sheets laminated together. This process is called smart-composite manufacturing and is the basis of the pop-up robotics paradigm [10]. Hinge designs consist of a central flexure supported by structural elements, with passive top and bottom flexure layers that are constrained to move within a confining sleeve (Fig. IVa-b). By limiting the translational motion of the flexure within the sleeve, we can control the angular stiffness profile (See Fig. IVc). A simple geometric relationship determines the angle at which point the stiffness changes, $\psi = t/\delta$, for a flexure that is offset from the center of rotation by layer thickness t , and allowed to translate within the sleeve a maximum distance δ .

To validate this hinge design we manufactured millimeter scale sleeve-hinges and micro-scale, flightworthy versions (Fig. IVb). We performed rotation-torque measurements on

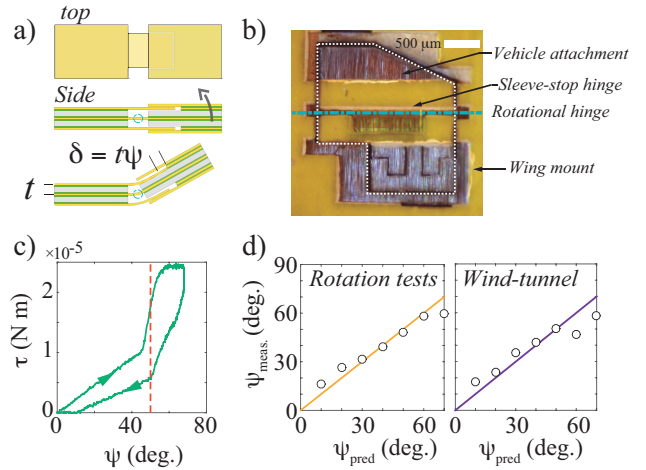


Fig. 6. Non-linear hinge manufacturing and testing. (a) Design of sleeve-stop hinges. (b) Laminate sleeve stop hinge for flapping wing vehicle. (c) Torque-rotation profile for a macro-scale hinge with stop angle set at 50° . (d) Comparison of desired and measured stop angle.

millimeter scaled hinges with varied stop angle using a custom rotation stage and force sensor. Analyzing the angle-torque relationship, we find that the angle at which point the stiffness change occurs matches the expected value given the geometry of the different hinges (Fig. IVd). To further validate this approach we placed 5×5 mm thin flat airfoil plates to the hinge. We subjected airfoil plates to aerodynamic loading in a wind tunnel and measured steady-state pitch angle as a function of velocity (see inset in Fig. 2). We find that hinges behave as expected from stress-strain tests, and under aerodynamic loading and are capable of maintaining fixed pitch angle over a wide range of aerodynamic pressure. As wind velocity was increased, the pitch angle reached a plateau at the desired stop angle (Fig. IVe). At very high speeds the hinges succumbed to buckling of the sleeve flexure layer and the hinge folded over (consistent with the upper plateau in the torque-angle curve in Fig. IVc).

IV. FLAPPING WING EXPERIMENTS

We performed yaw torque generation experiments with a two-actuator robobee mounted to a custom two-axis force sensor (Fig. 7). We constructed at-scale sleeve hinges designed to increase in stiffness a hinge angle of 40° . Experiments consisted of measuring the stroke-averaged drag force under varied split-cycle flapping. The system frequency and voltage were chosen to maximize stroke amplitude (approximately 60° peak to peak).

We measured yaw torque for three different wing hinge stiffness profiles: 1) an immobile hinge for constant C_D , 2) a flexible hinge with hinge stop, 3) an unbounded flexible wing with linear hinge stiffness. Consistent with our simple quasi-steady analysis, and our three-dimensional simulation, yaw control dynamics significantly differ when wing hinge is modified from stiff to flexible (Fig. 7b).

The stiff wing hinge results in a large, positive correlation between split-cycle parameter and yaw torque. This matches the analysis in which fixed wing hinges generate constant

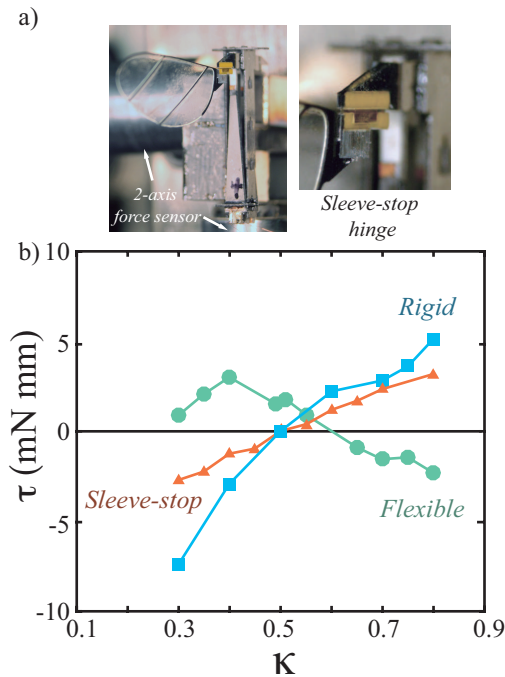


Fig. 7. a) Experiment overview of drag measurements on robobee. b) Torque versus split-cycle timing for three different wing hinges.

C_D across the stroke cycle, in which case the split-cycle paradigm produces optimum yaw torque. If we introduce partial flexibility through the hinge-stop mechanism, we observed a shallower, but still positive slope, for the yaw torque control relationship. In the final case, for a typical flexible wing hinge used to fly the robobee we see that yaw torque versus κ is opposite the rigid wing case, and consistent with the behavior of our previous analysis. The yaw torque control relationship for the flexible wing hinge is in the opposite direction than that of the rigid and soft-stop wing hinges.

V. CONCLUSIONS AND FUTURE WORK

Through a simple analytical model, three-dimensional simulations, and robot experiments we find that flexible wings can dramatically affect the production of asymmetric drag forces in flapping wing micro-aerial vehicles. The split-cycle control paradigm for generation of yaw torque is compromised by wing hinge flexibility. Passive wing rotation with linear hinges actually exhibit reduced drag force during the fast stroke of the split-cycle, and for operating points that maximize lift-to-drag, larger yaw torque is generated during the slow cycle.

The anomalous control phenomena observed in yaw are not likely to effect pitch and roll torque generation mechanisms because they do not rely on asymmetric wing velocities, which are at the root of the pitching dynamics. This matches our experience that operation of the robobee in free flight results in robust roll and pitch control while yaw authority is consistently lower [5], [6].

Our analysis highlights a more general point of interest

concerning the influence of flexible elements in flapping wing flight for biological and robotic systems. An alternative perspective to the yaw control problem analyzed here is that of the behavior of flexible wings under aerodynamic perturbations (i.e. changes in local velocity across the flexible wing). Our results suggest that passively flexing wings may aid in aerodynamic perturbation resistance by undergoing passive deflection. Thus wings that maintain passive, yet controllable elastic elements [13] may be advantageous for future design of robust yet stable flapping wing MAVs. Future work to explore how elastic and dissipative elements in biological and robotic flapping wings couple to the surrounding fluid and influence system dynamics will be essential to advance our knowledge and of flapping wing flight.

ACKNOWLEDGMENT

This work was supported by NSF (award number CCF-0926148), and the Wyss Institute for Biologically Inspired Engineering. Dr. Gravish acknowledges funding from the James S. McDonnell foundation. Any opinions, findings, and conclusions or recommendations expressed in this material are those of the authors and do not necessarily reflect the views of the National Science Foundation.

REFERENCES

- [1] Dario Floreano and Robert J Wood. Science, technology and the future of small autonomous drones. *Nature*, 521(7553):460–466, 28 May 2015.
- [2] Haithem E Taha, Ali H Nayfeh, and Muhammad R Hajj. Saturation-based actuation for flapping MAVs in hovering and forward flight. *Nonlinear Dyn.*, 73(1-2):1125–1138, 23 March 2013.
- [3] R J Wood, B Finio, M Karpelson, K Ma, N O Pérez-Arancibia, P S Sreetharan, H Tanaka, and J P Whitney. Progress on pico air vehicles. *Int. J. Rob. Res.*, 31(11):1292–1302, 1 September 2012.
- [4] Michael W Oppenheimer, David B Doman, and David O Sigthorsson. Dynamics and control of a biomimetic vehicle using biased wingbeat forcing functions. *J. Guid. Control Dyn.*, 34(1):204–217, 2011.
- [5] K Y Ma, S M Felton, and R J Wood. Design, fabrication, and modeling of the split actuator microrobotic bee. In *Intelligent Robots and Systems (IROS), 2012 IEEE/RSJ International Conference on*, pages 1133–1140, October 2012.
- [6] Kevin Y Ma, Pakpong Chirarattananon, Sawyer B Fuller, and Robert J Wood. Controlled flight of a biologically inspired, insect-scale robot. *Science*, 340(6132):603–607, 3 May 2013.
- [7] Stephen Nogar, Nogar Stephen, Serrani Andrea, Gogulapati Abhijit, and Jack J McNamara. Effect of wing flexibility and motor dynamics on Split-Cycle control of flapping wing vehicles. In *AIAA Guidance, Navigation, and Control Conference*, 2015.
- [8] J P Whitney and R J Wood. Aeromechanics of passive rotation in flapping flight. *J. Fluid Mech.*, 660:197–220, 10 October 2010.
- [9] C P Ellington. The aerodynamics of hovering insect flight. i. the Quasi-Steady analysis. *Philos. Trans. R. Soc. Lond. B Biol. Sci.*, 305(1122):1–15, February 1984.
- [10] J P Whitney, P S Sreetharan, K Y Ma, and R J Wood. Pop-up book MEMS. *J. Micromech. Microeng.*, 21(11):115021, 2011.
- [11] M H Dickinson. Wing rotation and the aerodynamic basis of insect flight. *Science*, 284(5422):1954–1960, June 1999.
- [12] G C H E de Croon, K M E de Clercq, Ruijsink, Remes, and C de Wagter. Design, aerodynamics, and vision-based control of the DelFly. *International Journal of Micro Air Vehicles*, 1(2):71–97, 2009.
- [13] Zhi Ern Teoh and R J Wood. A bioinspired approach to torque control in an insect-sized flapping-wing robot. In *Biomedical Robotics and Biomechatronics (2014 5th IEEE RAS EMBS International Conference on*, pages 911–917, August 2014.